5

Wavefront Propagation

M. Bowler, J. Bahrdt, and O. Chubar

Abstract. The modelling of photon optical systems for third generation synchrotrons and free electron lasers, where the radiation has a high degree of coherence, requires the complex electric field of the radiation to be computed accurately, taking into account the detailed properties of the source, and then propagated across the optical elements – so called wavefront propagation. This chapter gives overviews of two different numerical approaches, used in the wavefront propagation codes SRW and PHASE. Comparisons of the results from these codes for some simple test cases are presented, along with details of the numerical parameters used in the tests.

5.1 Introduction

In recent years, there has been an upsurge in the provision of new powerful sources of transversely coherent radiation based on electron accelerators. Free electron lasers (FELs) are providing coherent radiation from THz wavelengths to the ultraviolet, and there are projects in place to build FELs providing X-rays with the XFEL at HASYLAB in Hamburg, the Linear Coherent Light Source LCLS at Stanford and the Spring8 Compact SASE Source SCSS in Japan. Coherent synchrotron radiation (CSR) at wavelengths similar to or longer than the electron bunch is also produced by accelerating electrons. For CSR, the intensity is proportional to the square of the number of electrons in the bunch, hence very intense THz radiation is produced at bending magnets when the bunch length is of the order of a hundred microns, such as is required for FEL operation. Finally, the radiation from undulators, which provide the main sources of radiation in the new storage ring synchrotron radiation (SR) sources from UV to hard X-rays, has a high degree of coherence.

Traditionally, ray tracing, based on geometric optics, has been used to model the beamlines that transport the SR radiation from the source to the experiment. This has provided a sufficiently accurate model for most situations, although at the longer wavelength end of the spectrum some allowances for increased divergence of radiation due to diffraction at slits must be made.

For the coherent sources, interference effects are important as well as diffraction, and one needs to know the phase of the radiation field as well as the amplitude. Hence wavefront propagation, which models the evolution of the electric field through the optical system, is required.

The full solution of the Fresnel Kirchoff equation for propagating the field is possible, but it is computationally intensive and approximate solutions are sought. One approximation applicable to paraxial systems is to use the method of Fourier Optics. The code SRW (synchrotron radiation workshop) generates the source radiation field and also allows for its propagation across "thin" optics. This code is described in Sect. 5.2. Beamlines at UV and shorter wavelengths require highly grazing incidence optics, and in this case the thin optic assumption may not be appropriate. The Stationary Phase method is applicable in this regime and is used to approximate the propagation in the code PHASE, described in Sect. 5.3.

To cross-check both approximations, a Gaussian beam has been propagated across toroidal mirrors of different grazing angles and demagnifications, using both codes, and the size of the focal spots compared. These results are presented in Sect. 5.4 along with a study of the ability of both codes to handle astigmatic focusing.

SRW and PHASE have both been used to model the beamline for transporting THz radiation from the Energy Recovery Linac Prototype (ERLP) at Daresbury Laboratory. This is described in Sect. 5.5. Finally Sect. 5.6 summarizes the results and looks at future needs for wavefront propagation simulations.

The contribution of the COST P7 action has been in making two of these codes, PHASE and SRW, more widely known to the optics community, in running the test cases and in providing documentation to aid the new user. Two of the authors of these codes have joined with the COST P7 participants to write this chapter.

5.2 Overview of SRW

The SRW software project was started at the European Synchrotron Radiation Facility in 1997 [1]. The purpose of this project was to provide users with a collection of computational tools for various simulations involving the processes of emission and propagation of synchrotron radiation. The SRW code is composed of two main parts, SRWE and SRWP, enabling the following:

- Computation of various types of synchrotron radiation *emitted* by an electron beam in magnetic fields of arbitrary configuration, being considered in the near-field region (SRWE)
- CPU-efficient simulation of wavefront *propagation* through optical elements and drift spaces, using the principles of wave optics (SRWP).

Thanks to the accurate and general computation method implemented in SRWE, a large variety of types of spontaneous synchrotron emission by relativistic electrons can be simulated, e.g., radiation from central parts and edges of bending magnets, short magnets, chicanes, various planar and elliptical undulators and wigglers. Either computed or measured magnetic fields can be used in these simulations. Simple Gaussian beams can also be easily simulated. The extension of this part of the code to self-amplified spontaneous emission (SASE) and high-gain harmonic generation (HGHG) is currently in progress. An SRWE calculation typically provides an initial radiation wavefront, i.e., a distribution of the frequency-domain electric field of radiation in a transverse plane at a given finite distance from the source (e.g., at the position of the first optical element of a beamline), in a form appropriate for further manipulation.

After the initial wavefront has been computed in SRWE, it can be used by SRWP, without leaving the same application front-end. SRWP applies mainly the methods of Fourier optics, with the propagation of a (fully-coherent) wavefront in free space being described by the Fresnel integral, and the "thin" approximation being used to simulate individual optical elements – apertures, obstacles (opaque, semi-transparent or phase-shifting), zone plates, refractive lenses.

If necessary, the calculation of the initial electric field and its further propagation can be programed to be repeated many times (with necessary pre- and post-processing), using the scripting facility of the hosting front-end application.

5.2.1 Accurate Computation of the Frequency-Domain Electric Field of Spontaneous Emission by Relativistic Electrons

The electric field emitted by a relativistic electron moving in free space is known to be described by the retarded scalar and vector potentials, which represent the exact solution of the Maxwell equations for this case [2]:

$$\vec{A} = e\int_{-\infty}^{+\infty} \frac{\vec{\beta}}{R}\delta(\tau - t + R/c)\mathrm{d}\tau,\ \varphi = e\int_{-\infty}^{+\infty} \frac{1}{R}\delta(\tau - t + R/c)\ \mathrm{d}\tau, \quad (5.1)$$

where e is the charge of electron, c is the speed of light, $\vec{\beta} = \vec{\beta}(\tau)$ is the electron relative velocity, R is the distance between the observation point $\vec{r}$ and the instantaneous electron position $\vec{r}_{\mathrm{e}}(\tau)$, $R = |\vec{R}(\tau)|$, $\vec{R}(\tau) = \vec{r} - \vec{r}_{\mathrm{e}}(\tau)$, t is the time in laboratory frame, τ is the integration variable having the dimension of time, and $\delta(x)$ is the delta-function. The Gaussian system of units is used in (5.1) and subsequently.

One can represent the delta-function in (5.1) as a Fourier integral, and then differentiate the potentials (assuming the convergence of all integrals) to obtain the radiation field

$$\vec{E} = -\frac{1}{c}\frac{\partial \vec{A}}{\partial \tau} - \nabla\varphi = \frac{1}{2\pi}\int_{-\infty}^{+\infty} \vec{E}_\omega \exp(-\mathrm{i}\omega t)\,\mathrm{d}\omega,$$
$$\vec{E}_\omega = \frac{\mathrm{i}e\omega}{c}\int_{-\infty}^{+\infty}\left[\vec{\beta} - \left(1 + \frac{\mathrm{i}c}{\omega R}\right)\vec{n}\right]\frac{1}{R}\exp[\mathrm{i}\omega(\tau + R/c)]\mathrm{d}\tau, \tag{5.2}$$

where $\vec{E}_\omega$ is the electric field in frequency domain; $\vec{n} = \vec{R}/R$ is a unit vector directed from the instantaneous electron position to the observation point. We note that (5.2) has the same level of generality as (5.1), since no particular assumptions about the electron trajectory or the observation point have been made so far. One can show equivalence of (5.2) to the expression for the electric field containing the acceleration and velocity terms [3]. The exponent phase in (5.2) can be expanded into a series, taking into account the relativistic motion of the electron, and assuming small transverse components of the electron trajectory and small observation angles:

$$\tau + R/c \approx \frac{z - z_{\mathrm{e}0}}{c} + \frac{1}{2}\left[\tau\gamma_{\mathrm{e}}^{-2} + \int_0^\tau (x_{\mathrm{e}}'^2 + y_{\mathrm{e}}'^2)\mathrm{d}\tilde{\tau} + \frac{(x - x_{\mathrm{e}})^2 + (y - y_{\mathrm{e}})^2}{c(z - c\tau)}\right], \tag{5.3}$$

where γ_{e} is the reduced energy of electron ($\gamma_{\mathrm{e}} \gg 1$); $x,\ y,\ z$ are respectively the horizontal, vertical, and longitudinal Cartesian coordinates of the observation point $\vec{r}$; $x_{\mathrm{e}},\ y_{\mathrm{e}}$ are the transverse (horizontal and vertical) coordinates of the electron trajectory; $x_{\mathrm{e}}',\ y_{\mathrm{e}}'$ are the trajectory angles (or the transverse components of the relative velocity vector $\vec{\beta}$); and $z_{\mathrm{e}0}$ is the initial longitudinal position of the electron. The transverse components of the vector $\vec{n}$ in (5.2) can be approximated as

$$n_x \approx (x - x_{\mathrm{e}})/(z - c\tau),\ n_y \approx (y - y_{\mathrm{e}})/(z - c\tau). \tag{5.4}$$

The dependence of the transverse coordinates and angles of the electron trajectory on τ can be obtained by solving the equation of motion under the action of the Lorentz force in an external magnetic field. In the linear approximation this gives

$$(x_{\mathrm{e}},\ x_{\mathrm{e}}',\ y_{\mathrm{e}},\ y_{\mathrm{e}}')^{\mathrm{T}} \approx \mathbf{A}\cdot(x_{\mathrm{e}0},\ x_{\mathrm{e}0}',\ y_{\mathrm{e}0},\ y_{\mathrm{e}0}')^{\mathrm{T}} + \mathbf{B}, \tag{5.5}$$

where $(x_{\mathrm{e}0},\ x_{\mathrm{e}0}',\ y_{\mathrm{e}0},\ y_{\mathrm{e}0}')^{\mathrm{T}}$ is the four-vector of initial and instantaneous transverse coordinates and angles of the electron trajectory, $\mathbf{A} = \mathbf{A}(\tau)$ is a 4×4 matrix, and $\mathbf{B} = \mathbf{B}(\tau)$ is a four-vector with the components being scalar functions of τ.

Since the approximations used by (5.3) and (5.4) take into account the variation of the distance between the instantaneous electron position and the

observation point during the electron motion, the expression (5.2) with these approximations is valid for observations in the near field region.

Consider a bunch of N_e electrons circulating in a storage ring, giving an average current I. The number of photons per unit time per unit area per unit relative spectral interval emitted by such an electron bunch is

$$\frac{\mathrm{d}N_\mathrm{ph}}{\mathrm{d}t\mathrm{d}S(\mathrm{d}\omega/\omega)} = \frac{c^2\alpha I}{4\pi^2 e^3 N_\mathrm{e}} \left|\vec{E}_{\omega\mathrm{bunch}}\right|^2, \tag{5.6}$$

where $\vec{E}_{\omega\mathrm{bunch}}$ is the electric field emitted by the bunch in one pass in a storage ring, α is the fine structure constant. $\vec{E}_{\omega\mathrm{bunch}}$ can be represented as a sum of two terms describing, respectively, the incoherent and coherent synchrotron radiation [4]:

$$\left|\vec{E}_{\omega\mathrm{bunch}}\right|^2 \approx N_\mathrm{e} \int \left|\vec{E}_\omega(\vec{r};\mathrm{X_{e0}},\gamma_\mathrm{e0})\right|^2 \tilde{f}(\mathrm{X_{e0}},\gamma_\mathrm{e0})\mathrm{dX_{e0}}\mathrm{d}\gamma_\mathrm{e0} +$$
$$N_\mathrm{e}(N_\mathrm{e}-1)\left|\int \vec{E}_\omega(\vec{r};\mathrm{X_{e0}},z_\mathrm{e0},\gamma_\mathrm{e0}) f(\mathrm{X_{e0}},z_\mathrm{e0},\gamma_\mathrm{e0})\mathrm{dX_{e0}}\mathrm{d}z_\mathrm{e0}\mathrm{d}\gamma_\mathrm{e0}\right|^2, \tag{5.7}$$

where $\vec{E}_\omega$ is the electric field emitted by one electron with the initial phase space coordinates $x_\mathrm{e0},\ y_\mathrm{e0},\ z_\mathrm{e0},\ x'_\mathrm{e0},\ y'_\mathrm{e0},\ \gamma_\mathrm{e0}$, abbreviated to $\mathrm{X_{e0}}z_\mathrm{e0},\ \gamma_\mathrm{e0}$ in (5.7); f is the initial electron distribution in 6D phase space, normalized to unity; $\tilde{f} = \int f \mathrm{d}z_\mathrm{e0}$. The Stokes components of the spontaneous emission can be calculated by replacing the squared amplitude of the electric field in (5.7) with the corresponding products of the transverse field components or their complex conjugates.

5.2.2 Propagation of Synchrotron Radiation Wavefronts: From Scalar Diffraction Theory to Fourier Optics

Let us consider the propagation of the electric field of synchrotron radiation in free space after an aperture with opaque nonconductive edges. Using the approach of scalar diffraction theory, one can find the electric field of the radiation within a closed volume from the values of the field on a surface enclosing this volume by means of the Kirchhoff integral theorem [5]. After applying the Kirchhoff boundary conditions to the transverse components of the frequency-domain electric field emitted by one relativistic electron (see (5.2)), one obtains

$$\vec{E}_{\omega 2\perp}(\vec{r}_2) \approx \frac{\omega^2 e}{4\pi c^2} \int_{-\infty}^{+\infty} \mathrm{d}\tau \int_\Sigma \int \frac{\vec{\beta}_{\mathrm{e}\perp} - \vec{n}_{\mathrm{R}\perp}}{RS} \exp[\mathrm{i}\omega[\tau + (R+S)/c]]$$
$$(\vec{\ell}\cdot\vec{n}_\mathrm{R} + \vec{\ell}\cdot\vec{n}_\mathrm{S}) d\Sigma, \tag{5.8}$$

where $\vec{R} = \vec{r}_1 - \vec{r}_\mathrm{e},\ \vec{S} = \vec{r}_2 - \vec{r}_1$, with $\vec{r}_\mathrm{e}$ being the position of the electron, $\vec{r}_1$ a point at the surface Σ within the aperture, and $\vec{r}_2$ the observation point

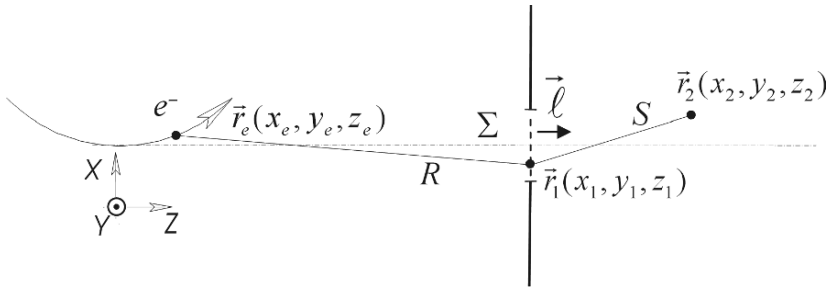

Fig. 5.1. Illustration of the Kirchhoff integral theorem applied to synchrotron radiation

(see Fig. 5.1). $S = |\vec{S}|$, $R = |\vec{R}|$, $\vec{n}_{\mathrm{R}} = \vec{R}/R$, $\vec{n}_{\mathrm{S}} = \vec{S}/S$, $\vec{\ell}$ is a unit vector normal to the surface Σ. The expression (5.8) is valid for $R \gg \lambda$, $S \gg \lambda$, where $\lambda = 2\pi c/\omega$ is the radiation wavelength. One can interpret (5.8) as a coherent superposition of diffracted waves from virtual point sources located continuously on the electron trajectory, with the amplitudes and phases of these sources dependent on their positions. This approach allows the calculation of complicated cases of SR diffraction, not necessarily limited by small observation angles.

In the approximation of small angles, the propagation of the SR electric field in free space can be described by the well-known Huygens–Fresnel principle [6], which becomes a convolution-type relation for the case of the propagation between parallel planes:

$$\vec{E}_{\omega 2\perp}(x_2, y_2) \approx \frac{\omega}{2\pi \mathrm{i} c L} \iint \vec{E}_{\omega 1\perp}(x_1, y_1) \exp\left[\frac{\mathrm{i}\omega}{c}[L^2 + (x_2 - x_1)^2 + (y_2 - y_1)^2]^{1/2}\right] \mathrm{d}x_1 \mathrm{d}y_1, \tag{5.9}$$

where $\vec{E}_{\omega 1\perp}$ and $\vec{E}_{\omega 2\perp}$ are the fields before and after the propagation and L is the distance between the planes. For efficient computation of (5.9), the methods of Fourier optics can be used.

The propagation through a "thin" optical element can be simulated by multiplication of the electric field by a complex transfer function T_{12}, which takes into account the phase shift and attenuation introduced by the optical element:

$$\vec{E}_{\omega 2\perp}(x, y) \approx \vec{E}_{\omega 1\perp}(x, y) T_{12}(x, y). \tag{5.10}$$

As a rule, the "thin" optical element approximation is sufficiently accurate for (nearly) normal incidence optics, e.g., for slits, Fresnel zone plates, refractive lenses, mirrors at large incidence angles, when the optical path of the radiation in the optical element itself is considerably smaller than distances between the elements or the distance from the last element to the observation plane.

For cases when the longitudinal extent of an optical element (along the optical axis) cannot be neglected, e.g., for grazing incidence mirrors, in particular when *the observation distance is comparable to the longitudinal extent of the optical element*, the "thin" approximation defined by (5.10) may need to be replaced by a more accurate method, which would propagate the electric field from a transverse plane just before the optical element to a plane immediately after it. Such propagators may be based on (semi-) analytical solutions of the Fourier integral(s) by means of asymptotic expansions. The general approach is still valid; the free-space propagator defined by (5.9) can be used immediately after the optic, followed by propagators through subsequent optical element(s), if any.

To take into account the contribution to the propagated radiation from the entire electron bunch, one must integrate over the phase space volume occupied by the bunch, treating the incoherent and coherent terms. For the simulation of incoherent emission (first term in (5.7)), one can sum up the intensities resulting from propagation of electric fields emitted by different "macro-particles" to a final observation plane. In many cases, like imaging by a thin lens, diffraction by a single slit, etc., the intensity in the observation plane is linked to the transverse electron distribution function via a convolution-type relation. In such cases the simulation can be accelerated dramatically. An alternative method for the propagation of the incoherent (partially-coherent) emission consists in manipulation with a mutual intensity or a Wigner distribution [6].

If the synchrotron radiation source is diffraction limited, the wavefront described by the first term in (5.7) is transversely coherent, and therefore it is sufficient to treat the propagation of the electric field emitted by only one "average" electron. Similarly, to simulate propagation of the coherent SR described by the second term in (5.7), it is also sufficient to manipulate with only one electric field wavefront, obtained after integration of the single-electron field over the phase space volume of the electron bunch.

5.2.3 Implementation

The emission part of the code (SRWE) contains several different methods for performing fast computation of various "special" types of synchrotron radiation. However, the core of the code is the CPU-efficient computation of the frequency-domain radiation electric field given by (5.2) with the radiation phase approximated by (5.3) in an arbitrary transversely uniform magnetic field.

The wavefront propagation in SRWP is based on a prime-factor 2D FFT. The propagation simulations are fine-tuned by a special "driver" utility, which estimates the required transverse ranges and sampling rates of the electric field, and re-sizes or re-samples it automatically before and after propagation through each individual optical element or drift space, as necessary for a given overall accuracy level of the calculation. In practice this means that running

SRWP is not more complicated than the use of conventional geometrical ray-tracing.

The SRW code is written in C++, compiled as a shared library, and interfaced to the "IGOR Pro" scientific graphing and data analysis package (from WaveMetrics). Windows and Mac OS versions of the SRW are freely available from the ESRF and SOLEIL web sites.

5.3 Overview of PHASE

In this section, we describe the principle of wavefront propagation within the frame of the stationary phase approximation. The method is complementary to the Fourier Optics technique with the following advantages:

- There is no ray tracing required across the optical elements as is needed in Fourier Optics. Hence, the method is valid also for thick lenses or long mirrors under grazing incidence angles.
- There are no restrictions concerning the grid spacing, the number of grid points, or the grid point distribution in the source and the image planes. One-dimensional cuts as well as images with small dimensions in one direction (e.g., monochromator slits with arbitrary shape) can be evaluated.
- Under certain conditions the propagation across several elements can be done in a single step.
- No aliasing is observed even for strongly demagnifying grazing incidence optics.
- The memory requirements are low.

The disadvantages are the following:

- The speed of simulation is significantly slower for the same number of grid points since the CPU time scales with N^4 rather than $N^2 \ln N$, with N being the number of grid points. On the other hand, the array dimension N needed to propagate $\pm 3\sigma$ of a Gaussian mode with a comparable resolution is generally much smaller as compared to Fourier Optics, which makes the CPU times of both methods comparable.
- The locations of the source plane and intermediate planes can not be chosen arbitrarily (see further).
- The description of the optical surface is restricted to low order polynomials, i.e., randomly distributed slope errors cannot be modelled.

The algorithm has been implemented into the code PHASE [7, 8]. The optical elements are described by fifth order polynomials. All expressions have been expanded up to fourth order in the image coordinates and angles. The FORTRAN code has been generated automatically using the algebraic code REDUCE [9].

Currently, PHASE is being rewritten to be used as a library within a script language. Several existing codes for pre- and post processing the electric fields will be included. This version will provide more flexibility to the user than the existing monolithic program.

5.3.1 Single Optical Element

In the following we assume a small divergence of the photon beam, which allows us to neglect the longitudinal field component. First, we will derive the transformation of the transverse field components from the source plane across a single optical element to the image plane (see Fig. 5.2 for the definition of the variables).

According to the Huygens–Fresnel principle the electric fields transform as

$$\vec{E}(\vec{a'}) = \int h(\vec{a'}, \vec{a})\vec{E}(\vec{a})\mathrm{d}\vec{a}, \tag{5.11}$$

where

$$h(\vec{a'}, \vec{a}) \propto \frac{1}{\lambda^2}\int_{\mathrm{Surface}} \frac{\exp(\mathrm{i}k(r+r'))}{rr'} b(w,l)\mathrm{d}w\mathrm{d}l, \tag{5.12}$$

$k = 2\pi/\lambda$ is the wave vector and $b(w,l)$ is the transmittance function of the optical element, which is not included in further equations. The propagator h includes the integration over the element surface. Principally, the propagator for two elements can be composed of the propagators of two individual elements in the following manner:

$$h(\vec{a''}, \vec{a}) = \int h_2(\vec{a''}, \vec{a'})h_1(\vec{a'}, \vec{a})\mathrm{d}\vec{a'}. \tag{5.13}$$

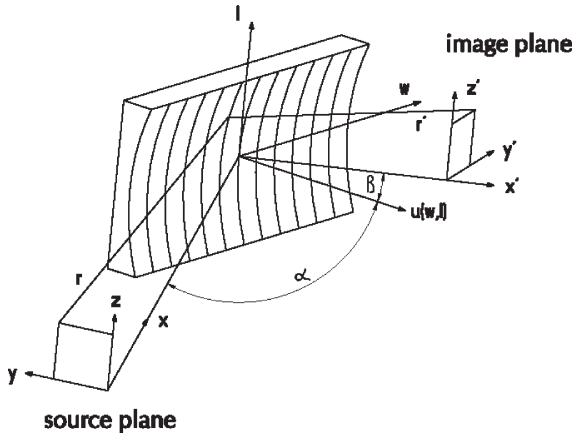

Fig. 5.2. Variables in the source and image plane and at the optical element

The total number of integration dimensions has increased to six, two dimensions for the surface integration over each element and two dimensions for the intermediate plane. The combined propagator can be rewritten in a way that the integration across the intermediate plane is skipped. This is justified since the beam properties are not modified at the intermediate plane. Therefore, the two element geometry requires two additional integrations as compared to the one element case. Each further optical element enhances the integration dimensions by two. Even for the one element geometry a simplification of the propagator is required to carry out the integration within a reasonable CPU time.

The integration over an optical element surface can be confined to a rather narrow region where the optical path length is nearly constant. If the path length changes rapidly, the integrand oscillates very fast and does not contribute to the integral.

We expand the propagator h around a principle ray where the optical path length PL has zero first derivatives with respect to the optical element coordinates and, hence, the phase variations are small.

$$h(\vec{a},\vec{a'}) \propto \frac{1}{r_{w_0,l_0} r'_{w_0,l_0}} \exp[\mathrm{i}k(r_{w_0,l_0} + r'_{w_0,l_0})] \int \exp[\mathrm{i}k(\frac{\partial^2 \mathrm{PL}}{\partial \delta w^2}\frac{\delta w^2}{2} + \frac{\partial^2 \mathrm{PL}}{\partial \delta l^2}\frac{\delta l^2}{2} + \frac{\partial^2 \mathrm{PL}}{\partial \delta w \partial \delta l}\delta w \delta l)]\mathrm{d}\delta w \mathrm{d}\delta l. \quad (5.14)$$

The quadratic form in δw and δl can be transformed to a normal form where the cross products vanish (principle axis theorem). Then, the double integral can be broken up into two integrals, which can be integrated analytically to infinity:

$$\int\int \cdots \mathrm{d}\delta w \mathrm{d}\delta l = \frac{2\pi \mathrm{i} \cdot \mathrm{sign}}{k\sqrt{|a| \cdot |b|}} = \frac{2\pi \mathrm{i} \cdot \mathrm{sign}}{k\sqrt{|D|}}, \quad (5.15)$$

where a and b are the principle axes. The determinant D is invariant for orthogonal transformations:

$$a \cdot b = D = \begin{vmatrix} \frac{\partial^2 \mathrm{PL}}{\partial \delta w^2} & \frac{\partial^2 \mathrm{PL}}{\partial \delta w \partial \delta l} \\ \frac{\partial^2 \mathrm{PL}}{\partial \delta l \partial \delta w} & \frac{\partial^2 \mathrm{PL}}{\partial \delta l^2} \end{vmatrix} \quad (5.16)$$

Thus, the integral can be solved analytically using the coefficients of the untransformed quadratic form. The second invariant of the quadratic form is the trace T and using D and T the expression *sign* can be evaluated:

sign $= 1$ if $T, D > 0$
sign $= -1$ otherwise

The surface integral of the propagator has been removed and the propagation now scales with the fourth power of the grid size N. This procedure is called

the stationary phase approximation [10] and it is justified as long as (1) the optical element does not scrape the beam and (2) the principle rays with identical source and image coordinates are well separated, which means that the quadratic approximation of the path length variation is valid. The latter constraint requires a careful choice of the location of the source plane in order to exclude a zero second derivative of the path length. A proper choice is indicated by a weak dependence of the results on small variations of the position of the source plane. The input data that are given for a certain longitudinal position can easily be propagated in free space to the source plane of the following PHASE propagation. This first step is done by Fourier optics.

For a sequence of optical elements it is useful to describe all expressions in terms of the coordinates and angles of the image plane, which we call initial coordinates in this context (the coordinates of the source plane are named final coordinates). The integration over the source plane is replaced by an integration over the angles of the image plane:

$$\vec{E}(\vec{a'}) = \int h(\vec{a'}, \vec{a})\vec{E}(\vec{a}) \left| \frac{\partial(y,z)}{\partial(\mathrm{d}y', \mathrm{d}z')} \right| \mathrm{d}(\mathrm{d}y')\mathrm{d}(\mathrm{d}z'). \tag{5.17}$$

The functional determinant containing the derivatives of the old with respect to the new coordinates is expanded in the initial coordinates $(y', z', \mathrm{d}y', \mathrm{d}z')$. Similarly, the expression $1/\sqrt{|D|}$ can be expanded in the same variables. These equations are the basis for the extension of the propagation method to several optical elements in the next section.

For narrow beams the path length derivatives can be replaced by

$$\left| \frac{\partial^2 \mathrm{PL}}{\partial \delta w^2} \frac{\partial^2 \mathrm{PL}}{\partial \delta l^2} - \left(\frac{\partial^2 \mathrm{PL}}{\partial \delta w \partial \delta l} \right)^2 \right| = \frac{\cos(\alpha)\cos(\beta)}{r^2 r'^2} \left| \frac{\partial(y,z)}{\partial(\mathrm{d}y', \mathrm{d}z')} \right|. \tag{5.18}$$

The expression on the right hand side can be generalized to a combination of several optical elements. There is, however, no obvious way to improve the accuracy of this substitution for wider photon beams.

Prior to the wavefront propagation, analytic power series expansions with respect to the initial coordinates $(y', z', \mathrm{d}y', \mathrm{d}z')$ of the five items listed in Table 5.1 are evaluated [7, 8]. Items 2 and 3 describe the phase advance $\Delta\Phi$ across the element:

$$\Delta\Phi = ((\mathrm{PL}(w_0, l_0) - \mathrm{PL}(0,0))/\lambda + \mathrm{mod}(w, 1/n))\, 2\pi, \tag{5.19}$$

where $1/n$ is the groove separation if the element is a grating. For mirrors the second term in the bracket is skipped. Items 4 and 5 are described by a common set of expansion coefficients and are multiplied together.

5.3.2 Combination of Several Optical Elements

Generally, the transformation of the coordinates and angles across an optical element is nonlinear. On the other hand, the transformation of all cross

Table 5.1. Quantities to be expanded with respect to the initial coordinates and angles

1	The final coordinates (y, z) in the source plane have to be known for the interpolation of the electric fields.
2	The path length differences which determine the phase variations of the principle rays.
3	The intersection points $(w_0,\ l_0)$ of the principle rays with the optical element are needed if the element is a diffraction grating.
4	The functional determinant relating source coordinates and image angles.
5	The expression $1/\sqrt{\lvert D\rvert}$ accounting for the surface integration.

products of the coordinates and angles is linear and can be described in a matrix formalism:

$$\begin{aligned}\overline{Y}_f &= \overline{\overline{M}} \cdot \overline{Y} i \\ \overline{Y}_{f/i} &= (y_{f/i}, z_{f/i}, \mathrm{d}y_{f/i}, \mathrm{d}z_{f/i}, {y_{f/i}}^2, y_{f/i} z_{f/i} \ldots).\end{aligned} \tag{5.20}$$

Expanding the products to fourth order the corresponding matrix has the dimensions of 70×70. First, the quantities 1–4 of Table 5.1 are derived for each optical element k. Then, the coordinates and angles of the intermediate planes are expressed by the coordinates and angles of the image plane of the complete beamline:

$$\overline{Y_m} = \left(\prod_{k=m+1}^{N} \overline{\overline{M_k}} \right) \cdot \overline{Y}_N = \overline{\overline{\aleph}} \cdot \overline{Y}_N. \tag{5.21}$$

Using these transformation maps the expressions 1–4 of Table 5.1 can be expanded with respect to the variables in the image plane of the beamline, e.g.,

$$\begin{aligned}\Delta\Phi_m &= \overline{\Delta\Phi_{Cm}} \cdot \overline{Y}_m = \overline{\Delta\Phi_{Cm}} \cdot \overline{\overline{\aleph}} \cdot \overline{Y}_N \\ w_{0m} &= \overline{wc_{0m}} \cdot \overline{Y}_m = \overline{wc_{0m}} \cdot \overline{\overline{\aleph}} \cdot \overline{Y}_N.\end{aligned} \tag{5.22}$$

The derivation of the fifth expression in Table 5.1 is more complicated. To account for all possible optical paths a $2N$-dimensional integral A has to be evaluated. Again, all cross terms are removed via a principle axis transformation from the coordinates $(\delta w_1,\ \delta l_1, \cdots \delta l_N)$ to the coordinates $(y_1, \cdots y_{2N})$ and the integral is solved analytically using the stationary phase approximation. The integral is related to the product of the eigenvalues $(\lambda_1,\ \lambda_2, \cdots \lambda_{2N})$ of the matrix $\overline{\overline{G}}$ (see (5.24)) via

$$\begin{aligned}A(w_{10}, l_{10}, \ldots w_{N0}, l_{N0}) = \frac{1}{\prod_{i=1}^{N+1} r_i} \frac{\partial(\delta w_1, \delta l_1 \cdots \delta l_N)}{\partial(y_1 \cdots y_{2N})} \cdot \\ \left(\frac{2\pi}{k}\right)^N e^{im\pi/4} - e^{-i(2N-m)\pi/4} \frac{1}{\sqrt{\lvert\lambda_1 \cdot \lambda_2 \cdots \lambda_{2N}\rvert}}.\end{aligned} \tag{5.23}$$

The expression $\partial(w_1,\ l_1 \cdots l_N)/\partial(y_1 \cdots y_{2N})$ equals one if the principle axis transformation is a pure rotation. m is the number of positive eigenvalues.

Using again the invariance of the determinant we get

$$\lambda_1 \cdot \lambda_2 \cdots \lambda_{2N} = \begin{vmatrix} g_{w_1w_1} & g_{w_1l_1} & g_{w_1w_2} & g_{w_2l_2} & \cdots & 0 \\ g_{l_1w_1} & g_{l_1l_1} & g_{l_1w_2} & g_{l_1l_2} & \cdots & 0 \\ g_{w_2w_1} & g_{w_2l_1} & g_{w_2w_2} & g_{w_2l_2} & \cdots & 0 \\ g_{l_2w_1} & g_{l_2l_1} & g_{l_2w_2} & g_{l_2l_2} & \cdots & 0 \\ \cdots & \cdots & \cdots & \cdots & \cdots & \cdots \\ 0 & 0 & 0 & 0 & \cdots & g_{l_Nl_N} \end{vmatrix}. \tag{5.24}$$

The expansion coefficients $g_{p_iq_j}$ represent the second derivatives of the path length with respect to the optical element coordinates p_i and q_j of the elements i and j. They are zero if $|p - q| > 1$. Each coefficient is a fourth order power series of the initial coordinates and angles and using these expansions the square root of the inverse of the determinant can be expanded with respect to the same variables. In principle m can be determined within an explicit derivation of all eigenvalues. We evaluate, however, only the determinant, the product of the eigenvalues, and we can only conclude from the sign of the determinant whether m is even or odd. A sign ambiguity of the integral A remains. This is acceptable since we are finally interested in the intensities rather than the amplitudes. For more details we refer to [11].

5.3.3 Time Dependent Simulations

So far we have discussed the propagation of monochromatic waves that are infinitely long. In reality, finite pulses with a certain degree of longitudinal coherence have to be propagated. The complete radiation field of an FEL can be generated with time dependent FEL codes like GENESIS [12]. Generally, these radiation pulses are described by hundreds or thousands of time slices where each slice describes the transverse electric field distribution at a certain time.

Prior to the propagation these fields have to be decomposed into their monochromatic components. For each grid point in the transverse plane the time dependence of the electric field is converted to a frequency distribution via an FFT. All relevant frequency slices (those for which the intensity is large and the frequency is not blocked by the monochromator) are then propagated as already described. The resulting frequency slices in the image plane are again Fourier transformed providing the time structure of the electric field in the image plane.

A detailed description of the longitudinal and transverse coherence of the FEL radiation is essential if the generation and the propagation of the radiation fields are combined. The spectral content and the time structure of the

FEL output can be modified by a monochromator as demonstrated in the following two cases:

- The signal-to-noise ratio of a cascaded HGHG FEL decreases quadratically with the harmonic number of the complete system. The output power of a four stage HGHG FEL can be significantly improved if the spectrum of the first stage is spectrally cleaned with a monochromator before it passes the following three stages. [13–15].
- The spectral power and purity of a SASE FEL can be enhanced by more than an order of magnitude using a self-seeding technique as proposed for the FLASH facility [16]. The SASE radiation of the first undulators that are operating far below saturation is monochromatized and used in the following undulators as a seed. Combined GENESIS and PHASE simulations have been performed for this geometry [17].

5.4 Test Cases for Wavefront Propagation

To compare the numerical methods used in SRW and PHASE, simple test cases looking at the focusing of Gaussian beams by a toroidal mirror have been carried out for a range of incident angles and demagnifications. For astigmatic optics, where the extent of the field is very different in different directions, it can be difficult to adequately represent the electric field, hence the tests were repeated using astigmatically focusing mirrors. The numerical parameters used in running the codes are given to assist new users.

5.4.1 Gaussian Tests: Stigmatic Focus

The optical system consists simply of a single toroidal mirror placed 10 m beyond the waist of a Gaussian radiation source. Focus distances of 10, 2.5, and 1 m were studied, giving demagnifications of 1, 4, and 10, respectively.

SRW was used to create the radiation field of a Gaussian beam of energy 2 eV, (wavelength 620 nm) with a waist of RMS size 212 μm at 1 m from the waist. Note that for Gaussian sources, the waist size is defined as $\sqrt{2}$ times the RMS size, that is, the input waist value was 300 μm. A small interface code was written to convert the format of the SRW field files to the input required for PHASE. Both codes could then be used to propagate the field along a 9 m drift space, across a toroidal mirror and then along a further drift space to the focus.

Numerical Set-Up

For propagation by SRW, the input field was generated using the automatic radiation sampling option, with an oversampling of 4, giving an input mesh for the propagation of 32×32 points over a 2 mm square. As a starting point for the propagation, automatic radiation sampling was used with the accuracy

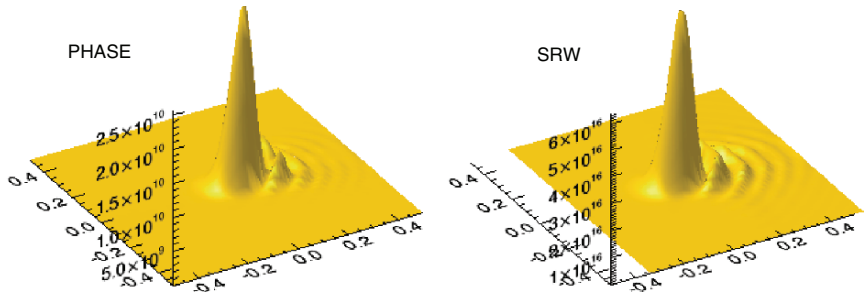

Fig. 5.3. Focal spot for the 87.5° incidence mirror, 10:1 demagnification. Intensities are in arbitrary units

parameter set to 4, and 100 × 100 points were used to define the mirror surfaces. However, for the optics with incidence angles of 85° and 87.5°, more points were required to define the mirror surface otherwise ghosting occurred in the image, and for the 10:1 demagnification the large number of points required to represent the field led to the code running out of memory when attempting to propagate the 1 m to the focal plane in 1 step. The focus shown in Fig. 5.3 for the 87.5° case with 10:1 demagnification was obtained using a grid of 2,000 by 2,000 points on the mirror, and propagating to the focus in three stages, resizing the beam at each stage.

For input to PHASE, a fixed grid of 51×51 points was used over the 2 mm square. PHASE requires the range and number of angles used to calculate the image to be set up (see Sect. 5.3.1). For the cases run above, the angular range used varied from ±5 mrads for unit magnification to ±25 mrads in the 10:1 demagnification case. One hundred and one angles were more than sufficient to give an accurate description of the field in the image plane.

Results

Horizontal and vertical cuts through the peak of the beam at the foci have been fitted using Gaussian functions. Table 5.2 compares the RMS sizes of the fitting functions for the PHASE and SRW calculations.

It can be seen that the focal spot sizes are in good agreement (<10%) except for the cases of 10:1 demagnification and the 4:1 demagnification for the most grazing system. It was found that this discrepancy is due to the principle rays not being well separated for highly demagnifying systems, thereby violating the conditions for the stationary phase approximation. The position of the source plane for PHASE can be altered so that the principle rays do not interfere; in this region the details of the image should be independent of the position of the source plane – see Sect. 5.3.1 and [11] for further details. Phase was rerun with the input source field calculated by SRW 1 m before the mirror and then propagated by PHASE. The new results are marked by superscript 1 in Table 5.2 and are in good agreement with those from SRW. The shape of the foci are similar, as can been seen from Fig. 5.3.

Table 5.2. Focal spot sizes from SRW and PHASE for a range of toroidal mirrors

Incidence angle (°)	Demagnification	Focal spot size SRW ($h \times v$) (μm)	Focal spot size PHASE ($h \times v$) (μm)
45	1	210×210	213×213
45	4	52.7×52.7	52.9×52.9
45	10	22.3×21.8	28.4×21.4
75	1	220×211	213×213
75	4	55.7×54.0	54.4×53.8
75	10	27.8×22.8	28.0×23.8
85	1	216×212	206×206
85	4	63.1×59.8	68.9×57.3
85	10	36.9×24.3	28.6×25.4
	10		35.8×27.2[1]
87.5	1	220×217	205×206
87.5	4	72.1×68.4	66.6×60.2
87.5	10	45.8×30.1	31.9×25.8
87.5	10		43.4×29.1[1]

[1] Result obtained by propagating field in PHASE from 1 m before mirror – see text

5.4.2 Gaussian Tests: Astigmatic Focus

The set-up for these tests is very similar to that described in the previous section, with a single toroidal mirror again placed 10 m from the Gaussian waist point. An incidence angle of 75° was chosen for these tests, with one focus either at 5.0 m or at 2.5 m from the mirrors, and the farther focus at 10 m.

Numerical Set-Up

For SRW, an accuracy parameter of 2 was used with the automatic sampling option for the propagation.

For PHASE, in the case of the 2:1 demagnification for the nearer line focus, a range of ±5 mrads was sufficient in order to reconstruct the wavefront at both line foci. For the farther focus, 301 angles were required in the nonfocused direction, whereas 201 were sufficient in the focused direction. In Fig. 5.4, the effect of using an insufficient number of angles can be seen in the distortion at the edge of the image.

Both programs in principle are able to handle astigmatic focusing. However, in PHASE, when the image plane is out of focus, the angles required to reconstruct the image and transverse position are strongly correlated, leading to an increase in the angle range needed over the whole image. This problem increases with the astigmatism. For the case of 4:1 demagnification at the nearer focus, a range of ±10 mrads was needed at the farther focus to reconstruct the image. However, this was required over a fine mesh of angles for the nonfocused direction, and the maximum number of angles allowed in the code was not sufficient to reconstruct the wavefunction. The inner focus at

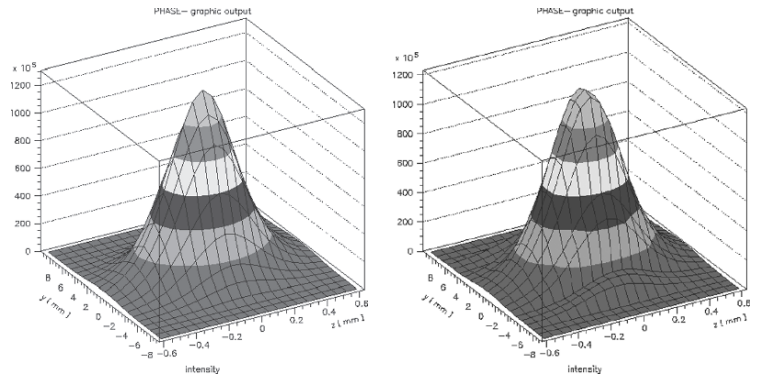

Fig. 5.4. Tangential line focus at 10 m from the toroidal mirror, which has the sagittal focus at 5 m. Left hand image used 301 angles in the nonfocusing direction, where the image on the right used 201 angles, and distortion at the image edge can be seen. Note the order of magnitude difference in the scales on the y and z axes

Table 5.3. Beam widths at the positions of the line foci for the astigmatically focusing toroidal mirrors

Distance to tangential focus (m)	Distance to sagittal focus (m)	Beam size at tangential $(h \times v)$ (μm)		Beam size at sagittal $(h \times v)$ (μm)	
		SRW	PHASE	SRW	PHASE
10	5	$212 \times 2{,}349$	$205 \times 2{,}269$	$1{,}118 \times 105$	$1{,}123 \times 102$
10	2.5	$212 \times 6{,}975$		$1{,}697 \times 52.6$	$1{,}635 \times 51.9$
2.5	10	$53.7 \times 1{,}713$	$54.9 \times 1{,}697$	$6{,}992 \times 212$	

2.5 m could be modeled using 501 points in the nonfocused direction over a ±10 mrads range.

This problem in PHASE can be solved by setting the distance, $d_$foc, from the image to the focal plane. The range of angles used is then centered around $y/d_$foc, where y is the transverse distance in the image plane, rather than centered round zero. In the version of the code used, this has been done for stigmatic focussing only, but can easily be extended to astigmatic systems.

Results

As before, horizontal and vertical cuts through the beam were fitted with Gaussian functions and the RMS widths are presented in Table 5.3. It can be seen that the agreement between PHASE and SRW is within 5% for the beam sizes at the foci where comparisons can be made. For SRW, the results with 2:1 and 4:1 demagnification in one direction are consistent with each other.

5.5 Beamline Modeling

PHASE has mainly been used to model the highly grazing incidence systems required for XUV and X-ray beamlines. The effect of diffraction gratings can also be included in PHASE as a phase shift across the wavefront. SRWP was designed for "normal incidence" geometries, and has been used for IR and THz wavelength beamlines. For these systems, the monochromator is not part of the beam transport system and SRW does not include any gratings. SRW has also been used for imaging X-rays using X-ray lenses and zone plates.

To compare the codes for modeling a real beamline, the THz beamline on the Energy Recovery Linac Prototype (ERLP) at Daresbury Laboratory [18] has been chosen as it had already been designed using SRW. This example extends the use of PHASE into a regime for which it was not originally designed.

5.5.1 Modeling the THz Beamline on ERLP

The Beamline

A 70 mrad fan of THz radiation will be extracted from ERLP where the electron bunch is shortest, i.e., at the last bend of the dipole chicane bunch compressor, just before the wiggler of the mid-infrared FEL. The THz radiation will be piped to a diagnostic room for analysis before being transported further to an experimental facility. The layout of the accelerator and beamlines is shown in Fig. 5.5; the beamlines have been constrained by the geography of the area, in particular the need to exit the machine room through a labyrinth resulting in the dog-leg in the beamline.

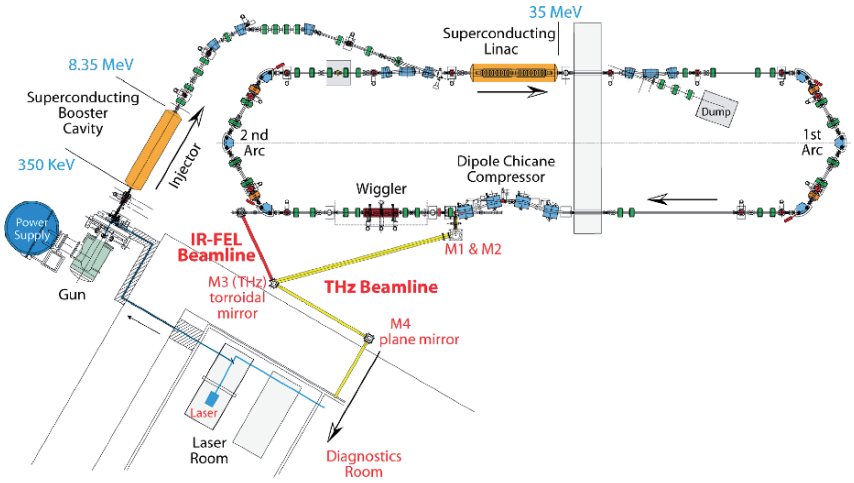

Fig. 5.5. Layout of ERLP, showing the paths of THz and IR-FEL beamlines

The main problem in designing this beamline is that, for longer wavelengths, diffraction becomes significant at the extraction aperture in the dipole magnet vacuum vessel and hence there is no single effective source point to image down the beamline. A second difficulty is that the radiation is naturally very divergent and, for the longer wavelengths, the mirrors will clip the radiation, giving rise to further diffraction.

To start from a known situation, the beamline has been designed to correctly focus the shorter wavelengths, which are not significantly diffracted by the extraction aperture. Two toroidal focusing mirrors, the first mirror (M1) after the aperture and the third mirror (M3) at the start of the labyrinth, are used in the transport path to the diagnostic room. There the radiation is collimated by a third toroidal mirror for input into a purpose-built large-aperture step-scan Fourier Transform Spectrometer. The mirrors have a diameter of 150 mm. The path length from the source to the collimating mirror is 17.3 m.

SRW was used to calculate the radiation emitted by the 35 MeV electrons at the 0.1 T bending magnet in the bunch compressor. The radiation field was generated just before the extraction aperture, at 0.659 m from the source point. Note that the intensity calculations are based on an average current, and so there is no account taken of the finite electron bunch length and hence there is as yet no allowance for the coherent enhancement of the radiation in SRW. Hence the intensities are in arbitrary units. Initial modelling was carried out at 62 μm (20 meV), for which diffraction is not important, to check that the mirror foci occurred at their nominal positions and the radiation could be well collimated. Propagation was then carried out at longer wavelengths, including 620 μm (2 meV) shown below. Of particular interest is the degree of collimation that can be obtained when there is no unique source point as described earlier.

Numerical Considerations

For propagation by SRW of the 620 μm radiation, the radiation field just before the extraction aperture plane was generated using automatic radiation sampling with an oversampling factor of 4. This generated 40×40 points over the initial grid of 45 mm by 45 mm. Propagation through the 37 mm diameter aperture and along the beamline to beyond the collimating mirror was done using the automatic field sampling option with the accuracy parameter set to 4.

For input into PHASE, a fixed grid of 51 by 51 points was used in SRW over the same 45 mm by 45 mm area and the output converted into PHASE field format. The aperture is included in PHASE by setting the radius of a pinhole in the input source plane, defined in the input parameter file (fg34.par). An angular mesh of 201 points over ±50 mrads was used for the propagation.

In PHASE, if the mirrors do not aperture the beam, the transformation across the whole beamline can be carried out in one step. This was done and

the results compared with those from SRW using large optics that do not clip the beam.

To allow for the finite size of the optics in PHASE, the beam should be propagated in stages to each aperturing optic, the radiation field output at the optic, and then used as the source for the next step in the propagation down the beamline, setting the source aperture appropriately. As the phase of the radiation field can vary rapidly, the field should be represented by its phase and amplitude, rather than by the real and imaginary parts. This has been done, e.g., by Bahrdt et al. [19] but not all the codes needed are generally available and hence the effect of the finite size of the mirrors was included using SRW alone.

Results

As the beam profiles are approximately Gaussian, cuts through the beam at three different locations were fitted with Gaussian functions. The RMS widths are presented in Table 5.4. It can be seen that the horizontal widths are in good agreement, but the vertical widths at the collimating mirror are about 15% larger from SRW than those from PHASE. This discrepancy is bigger than the variation of about 5% obtained when different sampling of the field is used. The origin of the difference has not yet been found.

The width of the 620 µm beam at the nominal focus of the first mirror, given in Table 5.4, is about an order of magnitude wider than the (correctly focused) 62 µm radiation. This results from the lack of a unique source to image down the beamline for the longer wavelengths. The effect on the collimation of the radiation can be seen by comparing the fitted beam widths at the collimating mirror and 2 m beyond; the 620 µm radiation after the "collimating mirror" is in fact converging. The percentage decrease in the beam size over the 2 m beyond the collimating mirror is very similar from both codes, and should be slow enough for FTIR measurements to be made. These simulations demonstrate the need to use wavefront propagation for systems where diffraction is important.

The effect of the finite mirror size was then investigated using SRW by setting the mirrors to $150 \times 150\,\mathrm{mm}^2$. The intensity distributions at and beyond

Table 5.4. Widths (RMS values) of Gaussian fits of horizontal and vertical cuts through the middle of the 620 µm beam at different locations in the beamline

Position in beamline	Horizontal width (mm)		Vertical width (mm)	
	SRW	PHASE	SRW	PHASE
At nominal "focus" of first mirror	10.9	11.1	12.0	11.3
At position of collimating mirror	38.1	37.0	43.9	36.9
2 m beyond collimating mirror	30.9	30.05	36.3	31.1

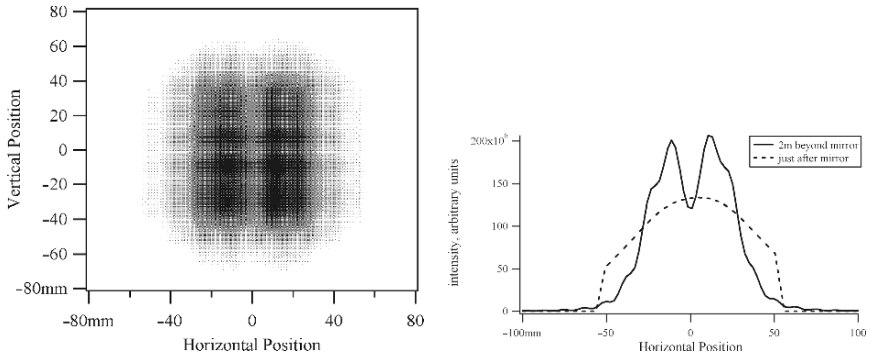

Fig. 5.6. (*LHS*) Image 2 m after the collimating mirror; (*RHS*) Horizontal cuts through the beam at and after the mirror, 620 μm radiation

the collimating mirror are shown in Fig. 5.6, where the diffraction due to significant clipping of the radiation by the collimating mirror is clearly seen. Since this work was carried out, the size of the collimating mirror has been increased to 200 mm.

5.6 Summary

Both methods for wavefront propagation, namely Fourier Optics and the Stationary Phase Approximation, are applicable to a wide range of situations. In general, Fourier techniques are fast, but can become more difficult to implement numerically for highly demagnifying systems. Good agreement was obtained between the results of SRW, which employs Fourier Optics, and PHASE even for highly grazing systems and 10:1 demagnification. Both codes are capable of handling astigmatic systems.

SRW and PHASE have between them been used very successfully to design a wide range of beamlines, from the transport of THz radiation to seeding schemes for XUV FELs. As coherent sources move to ever shorter wavelengths, further developments are required. More types of optical elements need to be included in the codes, in particular crystal optics. Work on wavefront propagation through crystals has for example been carried out by Mocella and co-workers [20] and Oreshko et al. [21]. The effect of imperfect surfaces, which introduce speckle and degrade micro and nanofocusing systems, also needs to be included.

References

1. O. Chubar, P. Elleaume, in *Proceedings of the 6th European Particle Accelerator Conference EPAC-98*, 1998, pp. 1177–1179
2. L.D. Landau, E.M. Lifshifts, *The Classical Theory of Fields*, (Pergamon Press, Oxford, 1975)

3. J.D. Jackson, *Classical Electrodynamics*, 3rd edn. (Wiley, New York, 1998)
4. S. Nodvick, D.S. Saxon, Phys. Rev. **96**, 180 (1954)
5. M. Born, E. Wolf, *Principles of Optics*, 4th edn. (Pergamon Press, New York, 1970)
6. K.-J. Kim, Nucl. Instrum. Methods A **246**, 71 (1986)
7. J. Bahrdt, Appl. Optics **34**, 114 (1995)
8. J. Bahrdt, Appl. Optics **36**, 4367 (1997)
9. A.C. Hearn, *REDUCE 3.5, A General Purpose Algebra System* (RAND, Santa Monica, CA, 1993)
10. L. Mandel, E. Wolf, *Optical Coherence and Quantum Optics*, (Cambridge University Press, Cambridge, 1995)
11. J. Bahrdt, Phys. Rev. Special Topics, Accel. Beams **10**, 060701 (2007)
12. S. Reiche, Nucl. Instrum. Methods A **429**, 243 (1999)
13. M. Abo-Bakr, R. Follath, A. Meseck, in *Proceedings of the 27th International FEL Conference*, Stanford, CA, 2005, pp. 19–22
14. K. Goldammer, A. Meseck, in *Proceedings of the 27th International FEL Conference*, Stanford, CA, 2005, pp. 23–26
15. J. Bahrdt, in *Proceedings of the 27th International FEL Conference*, Stanford, CA, 2005, pp. 694–710
16. J. Feldhaus, E.L. Saldin, J.R. Schneider, E.A. Schneidmiller, M.V. Yurkov, Opt. Comm. **140**, 341 (1997)
17. J. Bahrdt, B. Faatz, R. Treusch, V. Miltckev, R. Reininger, in *Proceedings of the 28th International FEL Conference*, Berlin, Germany, 2006, pp. 150–153
18. M.W. Poole, E.A. Seddon, in *Proceedings of the 9th European Particle Accelerator Conference EPAC-04*, Lucerne, 2004, pp. 455–457
19. J. Bahrdt, U. Flechsig, Proc. SPIE **3150**, 158 (1997)
20. V. Mocella, C. Ferrero, A.K. Freund, J. Hoszowska, L. Zhang, Y. Epelboin, Nucl. Instrum. Methods A **467**, 414 (2001)
21. A.P. Oreshko, V.A. Bushuev, D.V. Novikov, *Hasylab Annual Report* (2000)